

Steric effect induces enhancement of electroconvective flow near electrochemical interfacesQing Chen,¹ Hehua Zhu,² Peng Wang,^{3,4} and Wei Liu ^{4,5,*}¹Key Laboratory of Advanced Civil Engineering Materials, School of Materials Science and Engineering, Tongji University, Shanghai 201804, China²State Key Laboratory for Disaster Reduction in Civil Engineering, Tongji University, Shanghai 200092, China³Key Laboratory of Textile Science & Technology of Ministry of Education, College of Textiles, Donghua University, Shanghai 201620, China⁴School of Aerospace Engineering and Applied Mechanics, Tongji University, Shanghai 200092, China⁵Department of Engineering Mechanics, Tsinghua University, Beijing 100084, China

(Received 7 February 2024; revised 30 April 2024; accepted 30 May 2024; published 3 September 2024)

Electroconvection, occurring near electrochemical interfaces, propels the movement of ions and water, leading to intricate phenomena rooted in the fine interplay between fluid, voltage, and ion. Here, neglecting ionic interactions, by incorporating the steric term into the Poisson-Nernst-Planck-Stokes coupling equation, direct numerical simulations of electroconvective vortex near nanoslot-bulk interfaces are conducted. For the steric effect, the steric number is introduced to discuss the factors and laws affecting the vortex. We illustrate the substantial enhancement of electroconvective vortex due to the steric effect of ions within the nanoslot. Upon increasing the steric number, the cation concentration in the nanoslot is enhanced, resulting in the expansion of the electric double layer (EDL). The EDLs on the walls inside the nanoslot come into contact with each other, causing the EDLs to overlap, consequently increasing the total charge within the EDLs inside the nanoslot. This EDL overlap enhances the charge density of the extended space charge layer, leading to the enhancement of the electroconvective vortex. Further, our scaling analysis, corroborated by direct numerical simulation and existing data, establishes the scaling of slip velocity, jointly regulated by the steric number and voltage difference. By modulating the membrane transport characteristics, the steric effect reduces flow structure size and flux fluctuations, which offers new perspectives for manipulating ion transport and flow instability.

DOI: [10.1103/PhysRevE.110.035101](https://doi.org/10.1103/PhysRevE.110.035101)**I. INTRODUCTION**

Ion selective transport occurs on the electrochemical interfaces, generating an extended space charge (ESC) layer structure with localized peaks. The combined characteristics of low concentration electroconvection and high electric field hold vast potential applications in electrochemical domains such as seawater desalination [1], rectification [2], and electrodeposition [3]. Regarding the physical mechanism of vortices near electrochemical interfaces or ion-selective membranes, there are three possible explanations: (i) electroconvection (EC) associated with the ESC [4,5]; (ii) equilibrium EC related to the electric double layer (EDL) in depletion zone [6]; (iii) equilibrium EC associated with the EDL in preconcentration zone [7]. Here, our focus lies on EC near nanoslot-bulk interfaces, which are associated with the ESC.

In electrochemical or microfluidic systems, the transport of ions in a salt solution is driven by an externally applied electric field, and the ions are transported on an ion-selective surface. As a schematic, Fig. 1(a) shows the electrolyte near a cation-selective surface, which can be a negatively charged membrane or many nanochannels with negative surface charges. An applied electric field is used to push cations toward the ion-selective interface, while anions are pushed away from the ion-selective interface. Once the applied volt-

age increases to 20 times the thermal voltage, the electrolyte creates a strong concentration gradient perpendicular to the membrane surface [4,5]. Eventually, the region near the surface of the nanoslot-solution becomes highly depleted of ions. Due to the properties of the ion-selective membrane, only a small amount of cations are transported on the nanoslot-solution surface [Fig. 1(b)]. Thus, a large nonelectrically neutral region is formed in the spatial domain, which is called the ESC [4,5]. There is a strong electric field in the ESC region, and due to the slight roughness at the membrane interface, a tangential electric field can be induced on the surface of the nanoslot-solution. Under the action of the tangential electric field (E_y) and the normal electric field (E_x), the vortex is triggered on the membrane surface [Fig. 1(c)].

Up to now, there have been numerous studies related to EC associated with ESC, primarily focusing on linear stability analysis, statistical characteristics, and numerical simulation. Zaltzman and Rubinstein [4,6] conducted linear stability analyses on EC, finding that the onset voltage of vortices is jointly regulated by the Peclet number, diffusion coefficient, and wavelength. Mani and colleagues [8–10] observed that under high voltage, channels exhibit chaotic transport resembling turbulence, indicating that chaotic vortices can propel both positive and negative charges to splash into the bulk solution, resulting in a broadband spectral structure (similar to Rayleigh–Benard flow [11]). When altering the voltage loading path, EC exhibits supercritical and subcritical bifurcations. The bifurcation behavior has been systematically

*Contact author: mr_liuwei@tongji.edu.cn; mrliye@foxmail.com

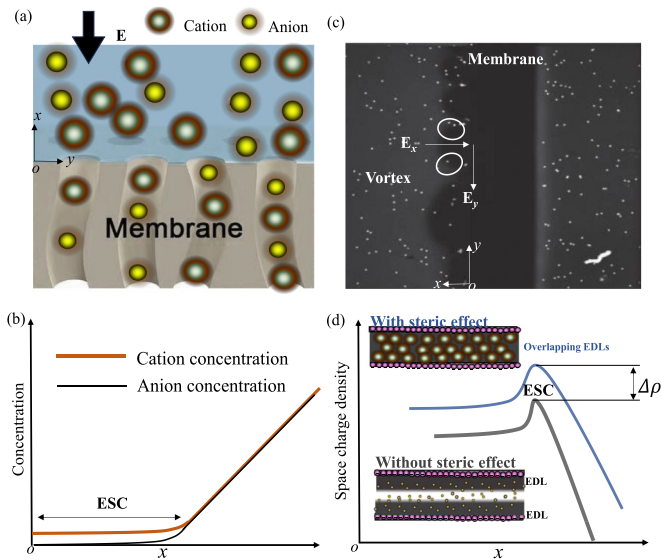


FIG. 1. Schematic diagram of steric effect induced enhancement of EC. (a) The formulation of the microfluidic system consists of a single ion-selective membrane (with a negatively charged nanoslot) and two bulk regions. (b) Ion concentration distribution near the membrane-solution interface. (c) Vortex structures form near the membrane [17]. (d) The diagram illustrates the enhancement mechanism of EC, achieved by adjusting the ESC structure, as it is closely associated with EC [4,5,6,26]. Taking into account the steric effect, the EDLs overlap increases the charge density of the ESC. However, when without steric effect, the charge density of the ESC is relatively lower. The schematic illustrations above and below illustrate the impact of the steric effect on the overlap of the EDL within the nanoslot and the enhancement of the charge density ($\Delta\rho$) of the ESC.

studied by Demekhin *et al.* [12,13], revealing that the bifurcation types are largely determined by the hydrodynamic coupling coefficient. Furthermore, the diffusion layer exhibits both linear and nonlinear evolution [14]. Subsequently, Pham *et al.* [15] discovered that changes in transverse electric fields and pressure gradients sustain vortices at low voltages, which is the mechanism behind subcritical bifurcation formation. Yossifon and Chang [16–18] experimentally observed intermittent vortex, demonstrating diffusion growth.

Modulation of EC is a hot topic. Studies have indicated that increasing shear flow velocity allows for the suppression of vortex morphology [19], height [20], and state [21]. Subsequently, Liu *et al.* [22] numerically discovered that under high voltage, the overlap of vortices leads to incomplete desalination regions shrinking along the inlet end, thereby achieving the physical phenomenon of vortex suppression by vortex. We further investigated the modulation of flow states by the ESC [23]. In many electrochemical applications, fluids can exhibit non-Newtonian fluid, which is often observed in lithium batteries. Li *et al.* [24] numerically investigated EC in viscoelastic electrolytes and found that polymer stretching promotes flow instability, depending on the Weissenberg number. Li *et al.* [25] also conducted numerical explorations on the influence of a magnetic field on EC. They discovered that applying a magnetic field can alter ion flux and EC through induced Lorentz forces, consequently reducing the size of flow structures. The aforementioned studies were conducted

in strong electrolyte systems; however, weak electrolytes are also prevalent in electrochemical systems. We showed that the Onsager effect in weak electrolytes can inhibit EC. This mechanism is rooted in the strong electric field within the ESC, which causes dissociation of weak electrolyte molecules, leading to the contraction of ESC structures, thereby achieving the inhibition of EC [26].

The modification of the pore structure of ion-selective membranes has been demonstrated to suppress EC, indicating a significant impact of membrane properties on EC [27]. Esfandiari *et al.* [28] demonstrated that increasing ion size alters the conductivity within strongly confined channels, implying a modulation effect of ion size on flow. In 1997, Borukhov *et al.* [29] proposed a transport equation considering ion size effect (steric effect), and found that increasing ion size weakens the concentration of cations within the EDL. The steric effect refers to the effect that ions are affected by the volume repulsion of the molecules around them during the transport process. This effect can cause the movement of ions in a channel or medium to be slowed or hindered. This effect is particularly significant when the ions size is close to the spatial confinement in the channel or medium. Subsequently, some scholars [30,31] delved into research on the ion size effect (steric effect) on EDL-associated electroosmosis within the framework of the Poisson-Boltzmann equation, rather than the Poisson-Nernst-Planck equation. They found that adjusting the hydration radius or ion concentration can significantly enhance EDL-related electroosmotic flow. Under the condition of ignoring flow, Zhang *et al.* [32] studied the influence of the steric effect on energy conversion in electrolyte-filled nanoslots and found that the coupling effect of the steric effect in EDL can strengthen the electric response of electrolyte solution-filled nanopores. This means that steric effects will become significant in nanoslots, but the effects of EC and ESC are not taken into account. For the study of EC that this article focuses on, EC is triggered on the nanoslot surface, which implies that the steric effect will significantly affect EC.

Herein, neglecting ionic interactions, we conduct direct numerical simulations (DNS) of a microfluidic system consisting of solution-membrane(nanoslot)-solution, incorporating the steric effect to explore its modulation on EC. Our findings indicate that steric effect can regulate the overlap of the EDLs within the nanoslot. Increasing steric effect leads to thicker wall EDL, intensifying EDLs overlap, and enhancing the charge density of the ESC [Fig. 1(d)]. Consequently, this induces an enhancement in EC. This control strategy is significantly different from shear control [20], polymer control [24], and buoyancy control [10].

II. THEORETICAL ANALYSIS WITH STERIC EFFECT

We considered that the computational geometry consists of a solution region, a nanoslot region, and a solution region, as shown in Fig. 2. When a large enough voltage is applied, it forms ESC and vortex near the ESC edge.

To analyze the steric effect within nanoslot on EC, all hydrated ions are treated as spherical particles. We demonstrate that the current simplified treatment can roughly reproduce the observed conductivity decay in experiments, see the Appendixes. Neglecting ionic interactions, based on

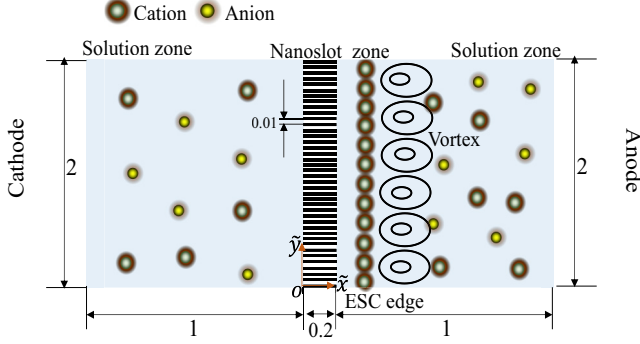


FIG. 2. Computational geometry, including solution zone, nanoslot zone (40 nanochannels), and bulk zone. The calculated dimensionless dimensions are noted in the figure.

the total free energy [29,33], we have

$$\begin{aligned}
 F = U - TS = \int dr & \left[-\frac{\varepsilon}{8\pi} |\nabla\varphi|^2 + z_1 e c_1 \varphi + z_2 e c_2 \varphi \right] \\
 & - \frac{k_B T}{a^3} \int dr [N_a c_1 a^3 \ln(N_a c_1 a^3) + N_a c_2 a^3 \ln(N_a c_2 a^3) \\
 & + (1 - N_a a^3 c_1 - N_a a^3 c_2) \ln(1 - N_a a^3 c_1 - N_a a^3 c_2)]. \quad (1)
 \end{aligned}$$

Here U is the electrostatic energy contribution, and $-TS$ is the entropy contribution; $\varepsilon = \varepsilon_0 \varepsilon_1$ is the dielectric constant, where ε_0 is the dielectric constant and ε_1 is the vacuum dielectric constant; φ is the voltage, e is the elementary charge, c_1 and c_2 are the ionic concentrations of K^+ and Cl^- ; k_B is the Boltzmann constant, T is the temperature and N_a is the Avogadro constant; $\mathbf{r} = (x, y)$ is the coordinates; a is the ion's radius; Thus, the modified Nernst-Planck equation can be expressed as follows $\frac{\partial c_i}{\partial t} = -\nabla \cdot (-D_i c_i \frac{\partial \varphi}{\partial c_i}) - \mathbf{U} \cdot \nabla c_i$, where \mathbf{U} is the velocity. The modified Nernst-Planck's equation is

$$\begin{aligned}
 \frac{\partial c_i}{\partial t} = D_i \nabla^2 c_i \pm D_i \frac{e}{k_B T} z_i \nabla \cdot (c_i \nabla \varphi) + N_a D_i a^3 \cdot \nabla \\
 \cdot \left(\frac{c_i \nabla (c_1 + c_2)}{1 - N_a \cdot a^3 \cdot c_1 - N_a \cdot a^3 \cdot c_2} \right) - \mathbf{U} \cdot \nabla c_i. \quad (2)
 \end{aligned}$$

In Eq. (2), $N_a \cdot D_i \cdot a^3 \cdot \nabla \cdot \left(\frac{c_i \nabla (c_1 + c_2)}{1 - N_a \cdot a^3 \cdot c_1 - N_a \cdot a^3 \cdot c_2} \right)$ describes the steric effect of ions size. z_i represents the valence of each ion. Eq. (2), third term on the right-hand side, describes the correction of ion concentration within the EDL in the nanoslot due to steric effect, which can influence the transport properties within the nanoslot.

The EC transport can be analyzed through the Navier-Stokes and Poisson-Nernst-Planck equations. The spatial coordinates, fluid velocity, pressure, time, ion concentration, and potential have been scaled to dimensionless values based on the channel height l_0 , diffusion velocity D_0/l_0 , diffusion time l_0^2/D_0 , bulk concentration c_0 , osmotic pressure $\mu D_0/l_0^2$, and thermal voltage $V_T = k_B T/e$. Here, D_0 represents the reference diffusion coefficient, and in our paper, a value of $D_0 = 10^{-9} m^2/s$ has been selected. Therefore, the following dimensionless forms of the Poisson-Nernst-Planck and

Navier-Stokes equation can be obtained:

$$\frac{\partial \tilde{c}_1}{\partial \tilde{t}} + \tilde{\nabla} \cdot \tilde{\mathbf{J}}_1 = 0, \quad (3)$$

$$\tilde{\mathbf{J}}_1 = -\tilde{\nabla} \tilde{c}_1 - \tilde{c}_1 \tilde{\nabla} \tilde{\varphi} - \tilde{\delta} \cdot \left(\frac{\tilde{c}_1 \tilde{\nabla} (\tilde{c}_1 + \tilde{c}_2)}{2 - \tilde{\delta} \tilde{c}_1 - \tilde{\delta} \tilde{c}_2} \right) + \tilde{\mathbf{U}} \cdot \tilde{c}_1, \quad (4)$$

$$\frac{\partial \tilde{c}_2}{\partial \tilde{t}} + \tilde{\nabla} \cdot \tilde{\mathbf{J}}_2 = 0, \quad (5)$$

$$\tilde{\mathbf{J}}_2 = -\tilde{\nabla} \tilde{c}_2 + \tilde{c}_2 \tilde{\nabla} \tilde{\varphi} - \tilde{\delta} \cdot \left(\frac{\tilde{c}_2 \tilde{\nabla} (\tilde{c}_1 + \tilde{c}_2)}{2 - \tilde{\delta} \tilde{c}_1 - \tilde{\delta} \tilde{c}_2} \right) + \tilde{\mathbf{U}} \cdot \tilde{c}_2, \quad (6)$$

$$\tilde{\nabla}^2 \tilde{\varphi} = -\frac{(\tilde{c}_1 - \tilde{c}_2)}{\tilde{\lambda}_D^2}, \quad (7)$$

$$0 = \tilde{\nabla}^2 \tilde{\mathbf{U}} - \tilde{\nabla} \tilde{P} - \tilde{\kappa} \frac{(\tilde{c}_1 - \tilde{c}_2)}{\tilde{\lambda}_D^2} \tilde{\nabla} \tilde{\varphi}, \quad (8)$$

$$\tilde{\nabla} \cdot \tilde{\mathbf{U}} = 0, \quad (9)$$

where \tilde{c}_1 and \tilde{c}_2 represent concentrations of cations and anions, respectively. $\tilde{\mathbf{J}}_1$ and $\tilde{\mathbf{J}}_2$ stand for fluxes of cations and anions, $\tilde{\varphi}$ denotes concentration, and $\tilde{\mathbf{U}}$ represents velocity, while \tilde{t} refers to time. The dimensionless Debye number $\tilde{\lambda}_D = \sqrt{\varepsilon k_B k / [(ze)^2 c_0]} / l_0$ indicates the ratio of the EDL size to the channel height l_0 . The literature reports that $\tilde{\lambda}_D$ is weakly sensitive to EC, here $\tilde{\lambda}_D$ is selected as 10^{-3} [8,10]. $\tilde{\kappa} = V_T^2 \varepsilon / (\mu D_0)$ represents the hydrodynamic coupling coefficient, describing the collective impact of diffusion coefficient D_0 , dielectric constant ε , and viscosity μ on the flow. In this study, we use a fixed value of $\tilde{\kappa} = 0.5$ [8]. Our main focus is on the influence of the following two key dimensionless parameters on EC:

$$\tilde{\delta} = 2N_a c_0 a^3, \quad (10)$$

$$\Delta \tilde{\varphi} = \frac{\Delta \varphi}{\frac{k_B T}{e}}. \quad (11)$$

The dimensionless number, $\tilde{\delta} = 2N_a c_0 a^3$, denotes the steric number, describing the equivalent volume fraction occupied by the total number of ions in unit concentration. N_a is the Avogadro constant (1/mol), c_0 is the bulk concentration (mol/L), and a is the hydrated ions radii (\AA). For Eq. (10), its dimension is 1. Although the dimensionless number (steric number) reported in Ref [33], has an expression of $\tilde{\delta} = 2c_0 a^3$, the units are mol. In addition, Ref. [33] neglected the contribution of the fluid and did not discuss the effect of EDLs overlap. The symbol $\Delta \tilde{\varphi}$ defines the ratio of the voltage difference ($\Delta \varphi$) across the system's two ends to the thermal voltage ($k_B T/e$).

To solve Eqs. (7)–(13) numerically, it is essential to define the respective boundary conditions. In nanoslot zone ($0 \leq \tilde{x} \leq 0.2$), the impermeable, no slip, and negative charge are considered, the corresponding boundary equations are as follows [34]:

$$\begin{aligned}
 \left(-\tilde{\nabla} \tilde{c}_1 - \tilde{c}_1 \tilde{\nabla} \tilde{\varphi} - \tilde{\delta} \cdot \left(\frac{\tilde{c}_1 \tilde{\nabla} (\tilde{c}_1 + \tilde{c}_2)}{2 - \tilde{\delta} \tilde{c}_1 - \tilde{\delta} \tilde{c}_2} \right) \right) \mathbf{n} = 0, \\
 \tilde{\mathbf{U}} = 0, \quad \tilde{\nabla} \tilde{\varphi} \cdot \mathbf{n} = \frac{l_0 \sigma}{\varepsilon V_T}, \quad (12)
 \end{aligned}$$

where \mathbf{n} is the unit outward normal vector in nanoslot, $l_0\sigma/\varepsilon V_T$ describes the dimensionless normal electric field strength generated by the negative charges. σ is the surface charge. Here, $\nabla\tilde{\varphi}\cdot\mathbf{n}$ is selected as -5×10^2 .

On the anodic side of the bulk zone ($\tilde{x}=1.2$), we assume a well-mixed concentration of both anions and cations, with no slip in velocity, and an applied voltage ($\Delta\tilde{\varphi}$). The corresponding boundary equation is as follows [34]:

$$\tilde{c}_1 = \tilde{c}_2 = 1, \quad \tilde{\mathbf{U}} = 0, \quad \tilde{\varphi} = \Delta\tilde{\varphi}. \quad (13)$$

Similarly, on the cathodic bulk boundary ($\tilde{x}=-1$), the corresponding boundary equation is as follows [34]:

$$\tilde{c}_1 = \tilde{c}_2 = 1, \quad \tilde{\mathbf{U}} = 0, \quad \tilde{\varphi} = 0. \quad (14)$$

The remaining lateral boundaries consider periodic boundary conditions for all field variables [4].

Next, we now derive the EC slip velocity considering the steric effect. Reference [4] reports an analytical solution for the charge density within the ESC ($0 \leq \tilde{x} < \tilde{x}_{\text{esc}}$) when neglecting the steric number, expressed as $\tilde{\rho} = \tilde{c}_1 - \tilde{c}_2 = \tilde{\lambda}_D \frac{\sqrt{\tilde{J}}}{\sqrt{2(\tilde{x}_{\text{esc}} - \tilde{x})}}$. Here, \tilde{x}_{esc} denotes the thickness of the ESC layer, identifiable by the location of the local peak within the ESC [refer to Fig. 4(d)]. \tilde{J} is the ion flux. The slip velocity of EC vortices originates from the ESC near the nanoslot-bulk interface [4,5]. Therefore, the slip velocity is closely related to the ESC layer. A detailed analysis of the ESC considering the steric effect is expected to provide a quantitative understanding of the steric number's impact on the slip velocity. As the ion size ($\tilde{\delta}$) increases, the concentration of cations at the nanoslot surface expands, resulting in an increase in the thickness of the EDL and the occurrence of EDLs overlap. Ignoring the steric effect, the scaling between the cation concentration within the nanoslot and the internal EDL thickness $\tilde{\lambda}_{D0}$ is given by $\tilde{c}_1 \sim \tilde{\lambda}_{D0}^2$ [35]. The steric effect refers to considering ions as nonideal spherical particles, leading to ion crowding within the nanoslot and approximated linear repulsion, resulting in a nearly linear increase between the nanoslot's Debye thickness $\tilde{\lambda}_{D1}$ and the steric number $\tilde{\delta}$. Therefore, we have $\tilde{\lambda}_{D1} \sim (\alpha\tilde{\delta} + 1)\tilde{\lambda}_{D0}$, where α represents a fixed fitting coefficient. Consequently, the cation concentration within the nanoslot satisfies $\tilde{c}_1 \sim (\alpha\tilde{\delta} + 1)^2 \tilde{\lambda}_{D0}^2 \sim (\alpha\tilde{\delta} + 1)^2$. Using $\tilde{\rho} \sim \tilde{c}_1$, we can obtain $\tilde{\rho} \sim (\alpha\tilde{\delta} + 1)^2$ because the space charge in the ESC all comes from the cation concentration. This approximate treatment approach originates from the local linear approximation in the literature [20,36] and was later confirmed by our DNS to be effective. For a given nanoslot, $\tilde{\lambda}_{D0}$ remains a constant (corresponding to $\tilde{\delta} = 0$). Therefore, we can obtain an approximate relation for the correction of ESC charge density:

$$\tilde{\rho} \sim (\alpha\tilde{\delta} + 1)^2 \tilde{\lambda}_D \frac{\sqrt{\tilde{J}}}{\sqrt{2(\tilde{x}_{\text{esc}} - \tilde{x})}}. \quad (15)$$

When $\tilde{\delta} = 0$, indicating no steric effect, the space charge density returns to the classical theoretical description [4]. Considering the steric effect of ions within the nanoslot, the ion accumulation leads to the overlap of EDLs. Consequently, more cations migrate into the ESC, thereby causing an increase in space charge density.

Integrating Eq. (15) twice within the ESC yields the voltage distribution within the ESC:

$$\frac{\tilde{\lambda}_D \tilde{\varphi}}{(\alpha\tilde{\delta} + 1)^2} \sim \frac{2\sqrt{2}}{3\tilde{J}} (\tilde{J}\tilde{x}_{\text{esc}})^{3/2} - \frac{(2\tilde{J}\tilde{x}_{\text{esc}} - 2\tilde{J}\tilde{x})^{3/2}}{3\tilde{J}}, \quad (16)$$

where \tilde{x}_{esc} represents the thickness of the ESC. Considering the balance between viscous forces and electrostatic body forces in the Stokes equation, we have

$$\frac{\partial^2 \tilde{v}}{\partial \tilde{x}^2} \sim \tilde{\kappa} \left(\frac{\partial^2 \tilde{\varphi}}{\partial \tilde{x}^2} \right) \frac{\partial \tilde{\varphi}}{\partial \tilde{y}}. \quad (17)$$

Therefore, substituting the voltage distribution from Eq. (16) into Eq. (17), we obtain

$$\begin{aligned} (\alpha\tilde{\delta} + 1)^{-4} \frac{\partial^2 \tilde{v}}{\tilde{\kappa} \partial \tilde{x}^2} &\sim -\frac{2\sqrt{2}}{3} \frac{(\partial \tilde{J} / \partial \tilde{y})}{\tilde{\lambda}_D \sqrt{\tilde{J}}} \\ &\times (\tilde{x}_{\text{esc}} - \tilde{x})^{3/2} \left(-\frac{\sqrt{2\tilde{J}}}{\tilde{\lambda}_D 2\sqrt{\tilde{x}_{\text{esc}} - \tilde{x}}} \right) \\ &= \frac{2}{3} \frac{1}{\tilde{\lambda}_D^2} (\partial \tilde{J} / \partial \tilde{y}) (\tilde{x}_{\text{esc}} - \tilde{x}). \end{aligned} \quad (18)$$

Integrating Eq. (18) and considering the boundary conditions $\partial \tilde{v} / \partial \tilde{x}|_{\tilde{x}=\tilde{x}_{\text{esc}}} = 0$ (please refer to Appendix E for more details on this shear-free boundary condition), we obtain

$$(\alpha\tilde{\delta} + 1)^{-4} \frac{\partial \tilde{v}}{\tilde{\kappa} \partial \tilde{x}} \sim \frac{1}{3\tilde{\lambda}_D^2} \frac{\partial \tilde{J}}{\partial \tilde{y}} (\tilde{x}_{\text{esc}} - \tilde{x})^2. \quad (19)$$

Integrating Eq. (19) and considering the no-slip boundary conditions yields

$$\tilde{v} \sim -\frac{1}{9} \tilde{\kappa} (\alpha\tilde{\delta} + 1)^4 \frac{1}{\tilde{\lambda}_D^2} \frac{\partial \tilde{J}}{\partial \tilde{y}} \tilde{x}_{\text{esc}}^3. \quad (20)$$

The expression for the slip velocity from Eq. (20) requires the solution for \tilde{x}_{esc} , which enables us to obtain the slip velocity at the edge of ESC. Assuming the voltage at the edge of the ESC is $\tilde{\varphi}_{\text{esc}}$ and at the nanoslot-solution interface is $\tilde{\varphi}_m$, based on the relation $\tilde{\varphi}(\tilde{x} = \tilde{x}_{\text{esc}}) - \tilde{\varphi}(\tilde{x} = 0) = \tilde{\varphi}_{\text{esc}} - \tilde{\varphi}_m$, we obtain

$$\tilde{x}_{\text{esc}} \sim \frac{\sqrt[3]{9}}{2} \tilde{\lambda}_D^{2/3} (\tilde{\varphi}_{\text{esc}} - \tilde{\varphi}_m)^{2/3} \tilde{J}^{-1/3}. \quad (21)$$

Substituting Eq. (21) into Eq. (20) yields

$$\tilde{v} \sim -\frac{1}{8} (\alpha\tilde{\delta} + 1)^{-4} \tilde{\kappa} \frac{\partial \tilde{J}}{\partial \tilde{y}} \tilde{J}^{-1} (\tilde{\varphi}_{\text{esc}} - \tilde{\varphi}_m)^2. \quad (22)$$

Reference [4] establishes the relationship between ion flux, dimensionless Debye number, ESC thickness, and voltage. It can be expressed as follows:

$$\begin{aligned} \frac{2\sqrt{2\tilde{J}}}{3\tilde{\lambda}_D} \tilde{x}_{\text{esc}}^{3/2} &\sim \tilde{\varphi} + \ln \left(\tilde{\lambda}_D \sqrt{\frac{2\tilde{J}}{\tilde{x}_{\text{esc}}}} \right) \\ &= \tilde{\varphi} + \ln(\tilde{\lambda}_D) + \frac{1}{2} \ln(2\tilde{J}) - \frac{1}{2} \ln(\tilde{x}_{\text{esc}}). \end{aligned} \quad (23)$$

When the voltage-current curve is in the overlimiting regime, the current satisfies $\tilde{J} \sim O(1)$. Since the dimensionless Debye number is much smaller than 1, we can ignore

$\tilde{\lambda}_D \tilde{\varphi}$, $\tilde{\lambda}_D \ln(\tilde{\lambda}_D)$, $\frac{1}{2} \tilde{\lambda}_D \ln(2\tilde{j})$. We have

$$\frac{2\sqrt{2\tilde{j}}}{3} \tilde{x}_{\text{esc}}^{3/2} \sim -\frac{1}{2} \tilde{\lambda}_D \ln(\tilde{x}_{\text{esc}}). \quad (24)$$

Note that \tilde{j} and \tilde{x}_{esc} are both functions of the position \tilde{y} . Differentiating Eq. (24) yields,

$$\frac{\partial \tilde{j} / \partial \tilde{y}}{\sqrt{\tilde{j}}} \cdot \tilde{x}_{\text{esc}}^{3/2} + 3\sqrt{\tilde{j}} \cdot \frac{\partial \tilde{x}_{\text{esc}}}{\partial \tilde{y}} \cdot \sqrt{\tilde{x}_{\text{esc}}} \sim -\frac{1}{2} \tilde{\lambda}_D \frac{\partial \tilde{x}_{\text{esc}} / \partial \tilde{y}}{\tilde{x}_{\text{esc}}}. \quad (25)$$

Dividing both sides of Eq. (25) by $\tilde{x}_{\text{esc}}^{3/2} / \sqrt{\tilde{j}}$ yields,

$$\frac{\partial \tilde{j} / \partial \tilde{y}}{\tilde{j}} + 3 \frac{\partial \tilde{x}_{\text{esc}} / \partial \tilde{y}}{\tilde{x}_{\text{esc}}} \sim -\frac{1}{2} \tilde{\lambda}_D \frac{\tilde{j}^{1/2}}{\tilde{x}_{\text{esc}}^{5/2}} \frac{\partial \tilde{x}_{\text{esc}}}{\partial \tilde{y}}. \quad (26)$$

Ignoring the lower-order terms in Eq. (26), we get,

$$\frac{\partial \tilde{j} / \partial \tilde{y}}{\tilde{j}} + 3 \frac{\partial \tilde{x}_{\text{esc}} / \partial \tilde{y}}{\tilde{x}_{\text{esc}}} \sim 0. \quad (27)$$

Substituting Eq. (27) into Eq. (22) and neglecting coefficients, we obtain the scaling form of the tangential slip velocity parallel to the nanoslot-bulk interface,

$$\tilde{v} \sim (\alpha \tilde{\delta} + 1)^4 \tilde{\kappa} (\tilde{\varphi}_{\text{esc}} - \tilde{\varphi}_m)^2 \frac{\partial \tilde{x}_{\text{esc}} / \partial \tilde{y}}{\tilde{x}_{\text{esc}}}. \quad (28)$$

Based on the linear approximation [20], $1/\partial \tilde{y} \sim 1/\tilde{d}_{ec}$, where \tilde{d}_{ec} is identified by the vortex height. We have

$$\tilde{v} \sim (\alpha \tilde{\delta} + 1)^4 \tilde{\kappa} (\tilde{\varphi}_{\text{esc}} - \tilde{\varphi}_m)^2 \frac{\tilde{x}_{\text{esc}} / \tilde{d}_{ec}}{\tilde{x}_{\text{esc}}}. \quad (29)$$

The dimensional vortex height d_{ec} was reported to follow a scaling law in Ref. [20], $d_{ec} \sim \sqrt{\frac{\varepsilon}{\mu}} (\Delta \tilde{\varphi}_1)$, where $\Delta \tilde{\varphi}_1$ represents the voltage difference. Based on the dimensionless reference values in this paper, the dimensionless form of the scaling law for vortex height can be obtained as $\tilde{d}_{ec} \sim \sqrt{\tilde{\kappa}} \Delta \tilde{\varphi}$. According to the reference, assuming the $\tilde{\varphi}_{\text{esc}}$ at vortex is approximately equal to the anode voltage [20,21], we have $\tilde{d}_{ec} \sim \sqrt{\tilde{\kappa}} (\Delta \tilde{\varphi} - \tilde{\varphi}_m)$. Therefore, under the condition of a fixed $\tilde{\kappa}$ [8], we obtain the scaling of the slip velocity considering steric effects:

$$\tilde{v} \sim (\alpha \tilde{\delta} + 1)^4 (\Delta \tilde{\varphi} - \tilde{\varphi}_m). \quad (30)$$

Equation (30) represents a key scaling in this paper. Upon increasing steric number $\tilde{\delta}$, the charge within the ESC increases. Hence, the physical interpretation of the scaling factor $(\alpha \tilde{\delta} + 1)^4$ is the contribution of steric effects-induced enhancement in space charge density to the slip velocity. The scaling factor $(\Delta \tilde{\varphi} - \tilde{\varphi}_m)$ signifies the contribution of the anode voltage and membrane voltage to the slip velocity. Especially, when $\tilde{\delta} = 0$, the scaling (30) reverts to the linear relation of slip velocity as observed in classical EC; see Fig. 4(c) of the Ref. [5].

III. DISCUSSION

For simulation parameters, for simplicity, this paper adopts the suggestions for ion parameter selection based on existing literature, treating the diffusion coefficients and ion radii of both positive and negative ions as single values [8,9,28,29,31].

These studies show that simplified strategies can effectively capture ion transport properties and flow patterns. Due to variations in particle size ($\mathcal{O}(1)[\text{\AA}] < a < \mathcal{O}(1)[\text{nm}]$) and concentrations ($\mathcal{O}(0.1)[\text{mM}] < c_0 < \mathcal{O}(10)[\text{mM}]$) across a wide range, we explore a spectrum of steric numbers, with $\tilde{\delta} \sim \mathcal{O}(0.1)$ [29–31,33]. Here we consider $0 \leq \tilde{\delta} \leq 0.4$ [29–31,33]. The voltage range is $0 \leq \Delta \tilde{\varphi} \leq 120$ [8]. Numerical solutions for the governing Eqs. (3)–(9) and the specified boundary conditions (12)–(14) are obtained using our finite element [7,22,23]. For the model validation and grid setup, please refer to Appendixes A and B.

A. Enhancement EC by steric effect

Figure 3(a) depicts a comprehensive visual representation of the steric effect. For comparison, we offer contrasting images considering the steric effect ($\tilde{\delta} = 0.4$) and when disregarding it ($\tilde{\delta} = 0$). It is revealing that the external electric field selectively propels ions within the nanoslot, forming an ion-depleted layer at the membrane (nanoslot) interface. This, in turn, prompts the development of an ESC layer, generating vortices near the nanoslot-solution interface. These small-scale vortices progressively transform into larger ones over time, which is generally consistent with experimental observations [17]. However, when accounting for the steric effect ($\tilde{\delta} = 0.4$), changes occur in the vortices at the nanoslot-solution interface, as illustrated at the bottom of Fig. 3(a).

We observed the situation of the internal EDLs within the nanoslot and found that considering the steric effect led to a significant overlap of EDLs. In contrast, without considering the steric effect, there is a minor overlap of EDLs, as shown in the magnified inset of Fig. 3(a). Thus the steric effect can alter the transport characteristics within the nanoslot, thereby modulating the EC near the nanoslot solution interface.

To quantify the enhancement of steric effects on EC, the spatiotemporal evolution of cation concentration at $\tilde{x} = 0.5$ [the dashed line in Fig. 3(a)] is analyzed, see Fig. 3(b). We observed that steric effects reduced the size of flow structures, leading to the presence of numerous fluctuating concentration plumes. This indicates a more intense rolling of vortices. However, without considering steric effects, we observed relatively larger-scale vortex structures, resulting in longer periods of fluctuating concentration plumes. The vortices rolling became more intense by considering steric effects, see Fig. 3(c). Figure 3(d) illustrates the impact of steric effects on ion flux, revealing that steric effects can attenuate ion flux. This is attributed to the steric effects inducing a steeper distribution of electric potential within the nanoslot. The intensified electric field leads to a sharp increase in the migration flux, surpassing the convective flux, consequently resulting in an overall reduction of the total ion flux within the system.

B. Physical mechanism of steric effect enhancing EC

It is well-recognized that EC originates ESC near the membrane-solution interface [4,5]. Therefore, the slip velocity of EC is directly linked to the ESC structure, which offers the physical understanding for enhancing EC. The effects of different steric numbers on ion concentration, potential, and charge density distribution are analyzed. In channels with

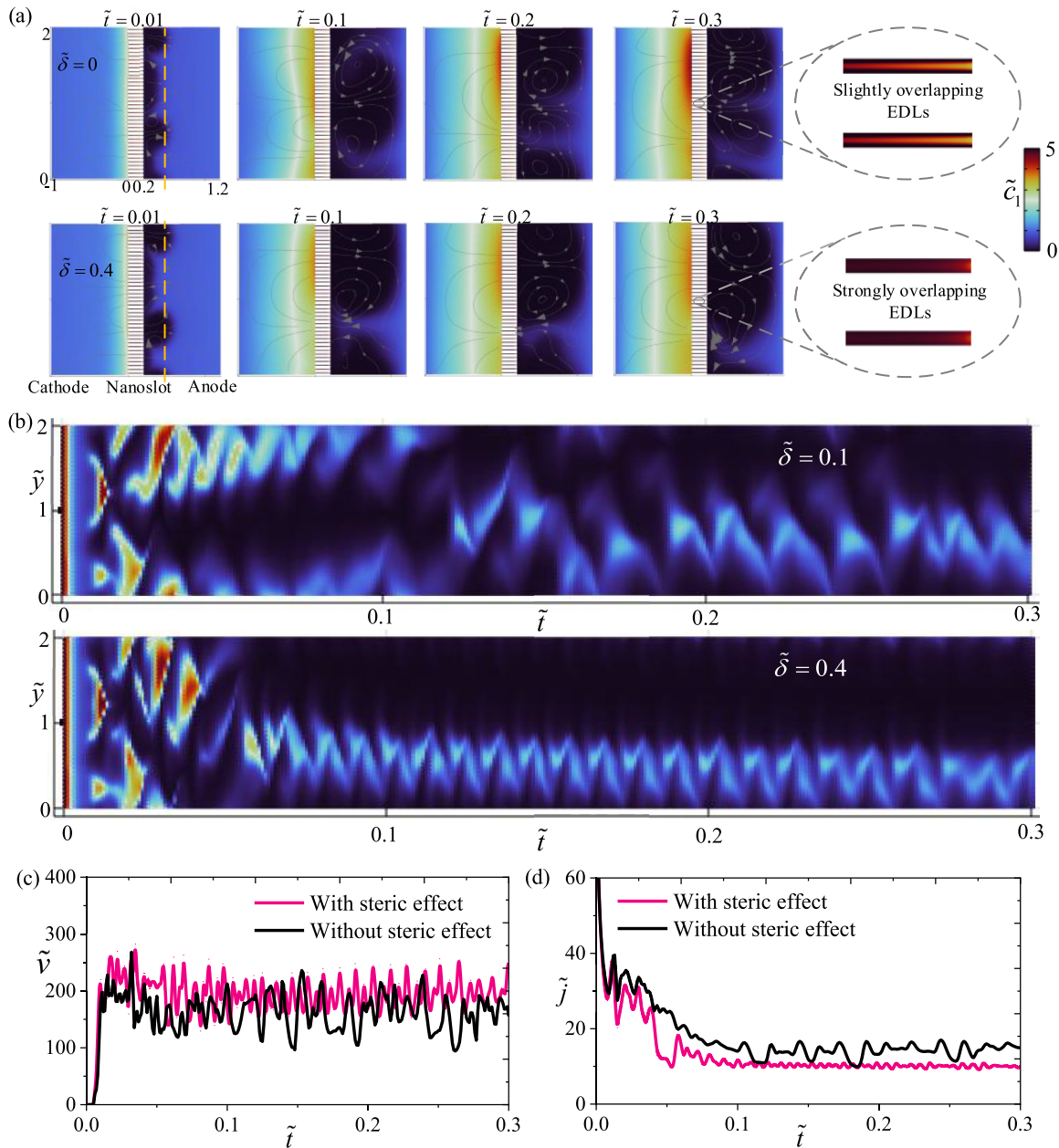


FIG. 3. Enhancement EC by steric effect. (a) Spatiotemporal evolution of EC without and with steric effects. The local zoom-in demonstrates the overlap status of EDLs within two adjacent nanoslot, indicating that steric effects can intensify the overlap of EDLs along the nanoslot walls. For more details, please see Appendix C. (b) Spatiotemporal evolution of cation concentration at $\tilde{x} = 0.5$ near the nanoslot-solution interface. (c) Effect of steric effect on ion flux. (d) Effect of steric effects on slip velocity. Ion flux \tilde{j} is calculated by subtracting the surface-averaged anion horizontal flux from the surface-averaged cation horizontal flux. The slip velocity \tilde{v} is defined by the maximum velocity at the ESC edge. Here, $\Delta\tilde{\varphi} = 100$.

weakly overlapping EDLs, as the steric number increases, the EDL thickness expands, leading to the overlap of wall EDLs. The overlapped EDLs further intensify the cation concentration within the nanoslot, transforming the concentration distribution curve from a sloped to a blocklike structure, as depicted in Fig. 4(a). Physically, ions within the nanoslot (membrane) are treated as spherical structures. Due to steric effects, the expansion of wall EDLs within the nanoslot induces EDLs overlap. As a consequence, the cation concentration is enhanced while the anion concentration decreases, as illustrated in Figs. 4(a) and 4(b). The steric effect induces

a more pronounced overlap of EDLs within nanoslot, suggesting a greater Donnan potential at the nanoslot-solution interface, as demonstrated in the local zoom-in of Fig. 4(c).

Under a strong electric field, cations within nanoslot are driven towards the bulk region, consequently leading to an increase in the charge density of the ESC [Fig. 4(d)]. Here, we did not observe any alteration in the ESC thickness due to the steric number, indicating that the steric number solely affects the charge density within the ESC. In summary, steric effects augment the charge density within the nanoslot solution interface's ESC, subsequently strengthening the volume force

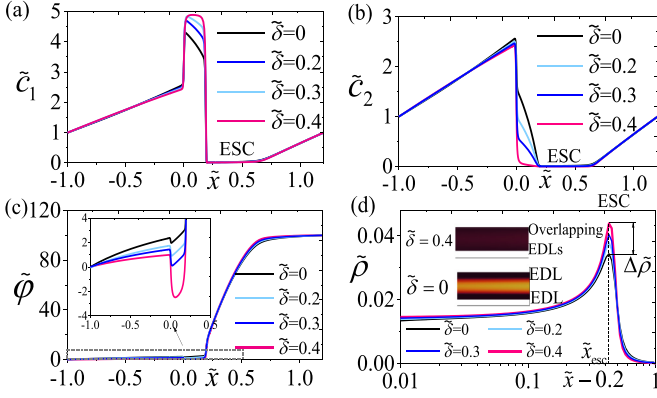


FIG. 4. Physical mechanism. The effect of the steric number on (a) cation concentration, (b) anion concentration, (c) potential, and (d) charge density. As the steric number increases, indicating larger volumes of ion spheres, it leads to the expansion of the two EDLs on the nanoslot surface, resulting in overlapping of EDLs. Here, $\Delta\tilde{\varphi} = 100$.

of the electric field, resulting in enhanced flow, as illustrated in Fig. 3.

C. Scaling of slip velocity with steric effect

Under the parameter space in this study ($0 \leq \Delta\tilde{\varphi} \leq 120$ and $0 \leq \tilde{\delta} \leq 0.4$), the slip velocity increases with the rise in steric numbers. Utilizing the scaling $(\alpha\tilde{\delta} + 1)^4 (\Delta\tilde{\varphi} - \tilde{\varphi}_m)$, all scattered data points collapse onto our theoretical line, as depicted in Fig. 5(a). The fitting coefficient α is approximately 0.41. When $\Delta\tilde{\varphi} = 100$, the slip velocity increases from 144.65 ($\tilde{\delta} = 0$) to 208.19 ($\tilde{\delta} = 0.4$), resulting in a slip velocity enhancement of 43.92%. The physical significance of the scaling factor $(\alpha\tilde{\delta} + 1)^4$ is the contribution of the steric effect enhancing the ESC charge density to the slip velocity. The scaling factor, $\Delta\tilde{\varphi} - \tilde{\varphi}_m$, represents the contribution of voltage drop in the vortex region to the slip velocity. Specifically, when $\tilde{\delta} = 0$, the system reverts to the classical EC [5,8,37]. The mechanism by which the steric effect enhances the slip velocity depends on the enhancement of the ESC charge density. Therefore, using the scaling $(\alpha\tilde{\delta} + 1)^2$, the dispersed peaks in Fig. 4(d) of this paper collapse into a single point; see Fig. 5(b).

IV. CONCLUSION

In this paper, we conducted the DNS of the EC system composed of solution-nanoslot-solution, and unveiled the enhancement of EC by steric effect. The steric effect induces the overlap of EDLs within the nanoslot, prompting a greater migration of cations toward the ESC, thereby intensifying EC. Our scaling analysis revealed the quantitative regulation of slip velocity evolution by steric effect, supported by existing data and our DNS. This work extends our understanding of the steric effect modulated EC, offering new avenues for manipulating ion transport and controlling instabilities in electrochemical applications. In addition, our analysis is performed on the diffusion coefficients and ion size with the fixed value, which is a limitation of the hypothetical scenario. The asymmetric effect of the diffusion coefficients and ion

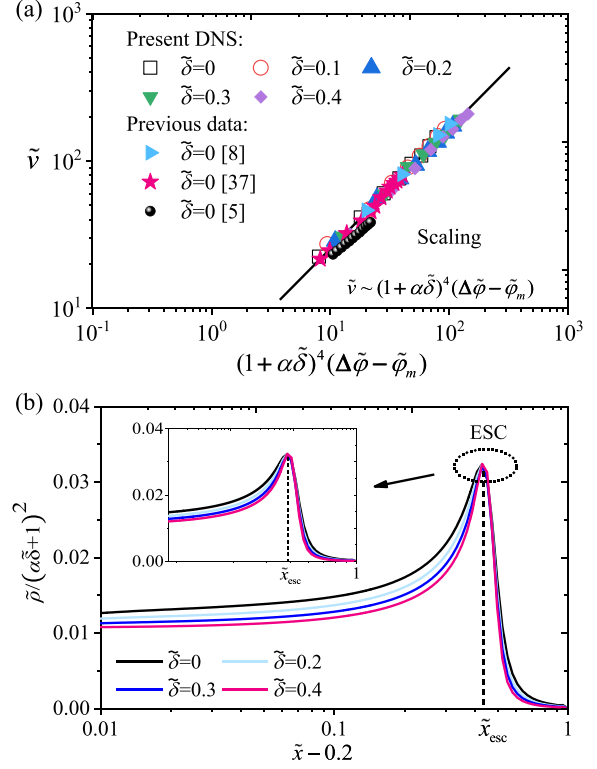


FIG. 5. Scaling law. (a) Slip velocity of the vortex plotted against the scaling $(\alpha\tilde{\delta} + 1)^4 (\Delta\tilde{\varphi} - \tilde{\varphi}_m)$. Here, the previous data is extracted from Fig. 4(c) in Ref [5], Fig. 5(a) in Ref [8], and red line of Fig. 9(b) in Ref [37]. Please refer to Appendix D for data points. (b) The scaling behavior of the convex peak of the ESC.

size may be interesting, and theoretical studies on it deserve to be conducted in future work.

ACKNOWLEDGMENTS

We thank Prof. B. Zaltzman at Ben-Gurion University of the Negev, Prof. D. Deng at Fudan University, and Prof. M. Zdenek Bazant at Massachusetts Institute of Technology for their helpful comments on the earlier draft. We also thank two anonymous reviewers for their helpful comments. This work was financially supported by National Key Research and Development Projects No. 2022YFC3803104, National Natural Science Foundation of China No. 52078381, No. 51878496, No. 52122808, No. 51878480, No. 52078369, No. U22B2076, and No. 51878481, the MITT's 2021 Public Service Platforms for Industrial Technology Foundation (2021-H029-1-1), Program of Shanghai Academic Research Leader (22XD1403300), China Postdoctoral Science Foundation (No. 2023M741970), Postdoctoral Fellowship Program of CPSF (No. GZB20230361), and Fundamental Research Funds for the Central Universities.

The authors report no conflicts of interest.

APPENDIX A: GRID SETTINGS

The spatial discretization of the governing equations was performed using both quadrilateral and triangular grids, with extreme grid refinement near the nanoslot-bulk interfaces and

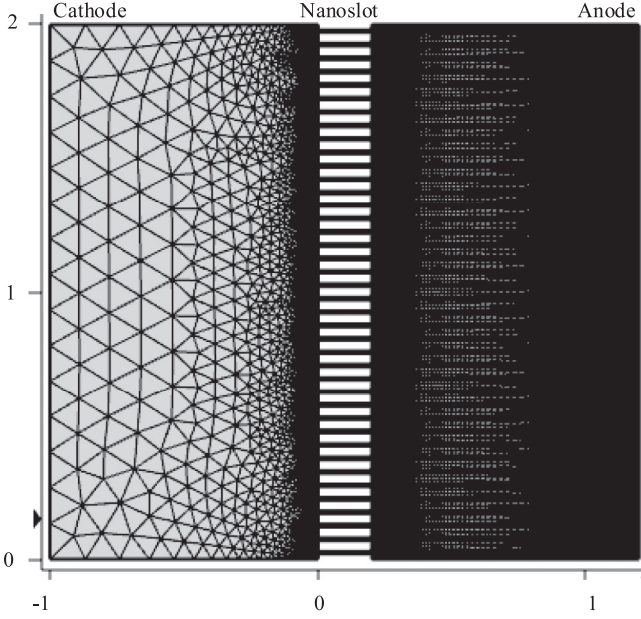


FIG. 6. Grid configuration. Triangular grids are utilized in the enriched region on the left, while quadrilateral grids are employed in the membrane (nanoslot) region in the middle and the depleted zone on the right.

in the vicinity of nanoslots to address the transport issues caused by space charges, as illustrated in Fig. 6. The maximum grid size within the EDL was restricted to $\mathcal{O}(0.1\tilde{\lambda}_D)$, whereas at the nanoslot-bulk interfaces, the minimum grid size was $\mathcal{O}(0.1\tilde{\lambda}_D)$, with a maximum grid size of $\mathcal{O}(10\tilde{\lambda}_D)$. To assess the relationship between simulation results and grid density, we conducted a systematic analysis across different grid spacings ranging from $\mathcal{O}(0.01\tilde{\lambda}_D)$ to $\mathcal{O}(100\tilde{\lambda}_D)$. Numerical results indicate that coarser grid settings yield sub-optimal computational outcomes. Conversely, excessively fine grids significantly diminish computational efficiency. However, maintaining maximum grid sizes within the EDL and ESC at $\mathcal{O}(0.1\tilde{\lambda}_D)$ and $\mathcal{O}(10\tilde{\lambda}_D)$, respectively, exhibits robust convergence. This grid setting method can smoothly capture concentration, voltage and flow fields. In addition, since there are no vortices in the bulk region on the cathode side, the grid only needs to resolve the EDL in the enriched region, and the minimum grid is set to $\mathcal{O}(0.1\tilde{\lambda}_D)$.

APPENDIX B: BENCHMARKS

We discuss the validation of numerical test cases. Reference [28] reported on the influence of ion size on the conductivity within channels, noting that larger ion sizes corresponded to reduced conductivity within the channel. This paper simplifies the treatment of ions as spherical particles, which roughly replicates the observed conductivity decay in experiments, as depicted in Fig. 7(a). However, in scenarios of weak overlap, steric effects can promote the overlapping of EDLs, as discussed in the main manuscript. Here, it is essential to note that the reported confined channel has a dimension of only $\mathcal{O}(0.1)$ nm, a dielectric constant of 2, and a bulk concentration of $\mathcal{O}(1)$ mM. Under such conditions, the dimensionless Debye number, $\tilde{\lambda}_D$, is at the order of $\mathcal{O}(1)$,

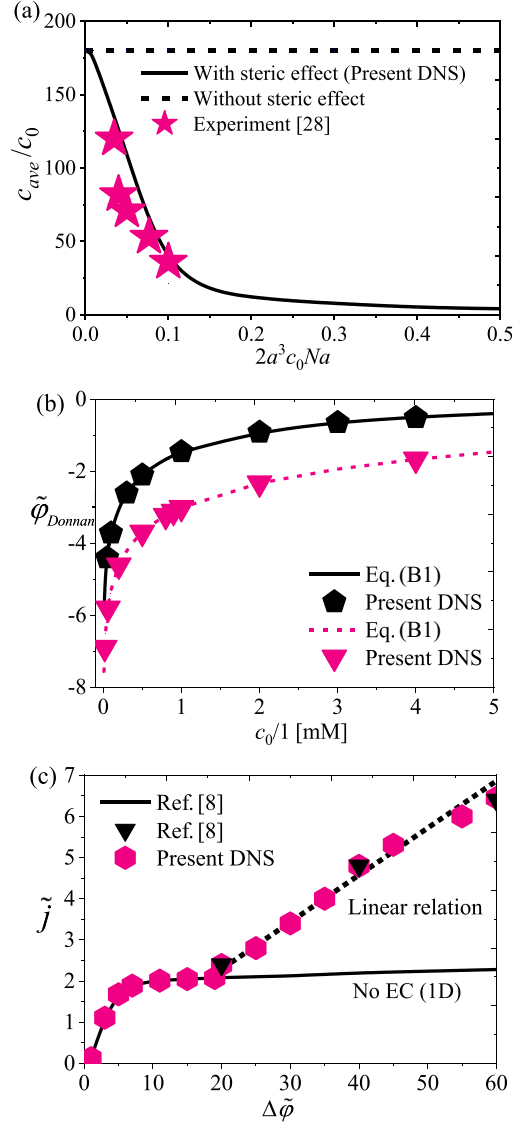


FIG. 7. Benchmarks. (a) Under the influence of an external electric field and considering steric effects, a comparison of the average cation concentration within the nanochannel. Here $\Delta\tilde{\phi} = 10$. (b) Under zero electric field conditions and neglecting steric effects, a quantitative comparison between the Donnan potential and the analytical solution. The solid line represents simulation parameters with $\sigma = -1[\text{mC}/\text{m}^2]$ and $H = 5[\text{nm}]$, while the dashed line represents simulation parameters with $\sigma = -10[\text{mC}/\text{m}^2]$ and $H = 10[\text{nm}]$. (c) Neglecting steric effects, a quantitative comparison of voltage-current curves with existing data [8].

indicating a significant overlap of double layers within the membrane pores. To ensure the validity of the fundamental continuity theory in this paper, we utilized nanochannels with heights greater than $\mathcal{O}(10)$ nm. By reducing the bulk concentration [to $\mathcal{O}(0.01)$ mM], we brought $\tilde{\lambda}_D$ into a range more consistent with the experimental setup, allowing for the normalization of obtained data results. Such an analysis is commonly encountered in fluid mechanics analyses. Considering the effect of ion size, in situations of significant overlap of EDLs, the number of ions accommodated within the nanoslot decreases with an increase in ion volume. This

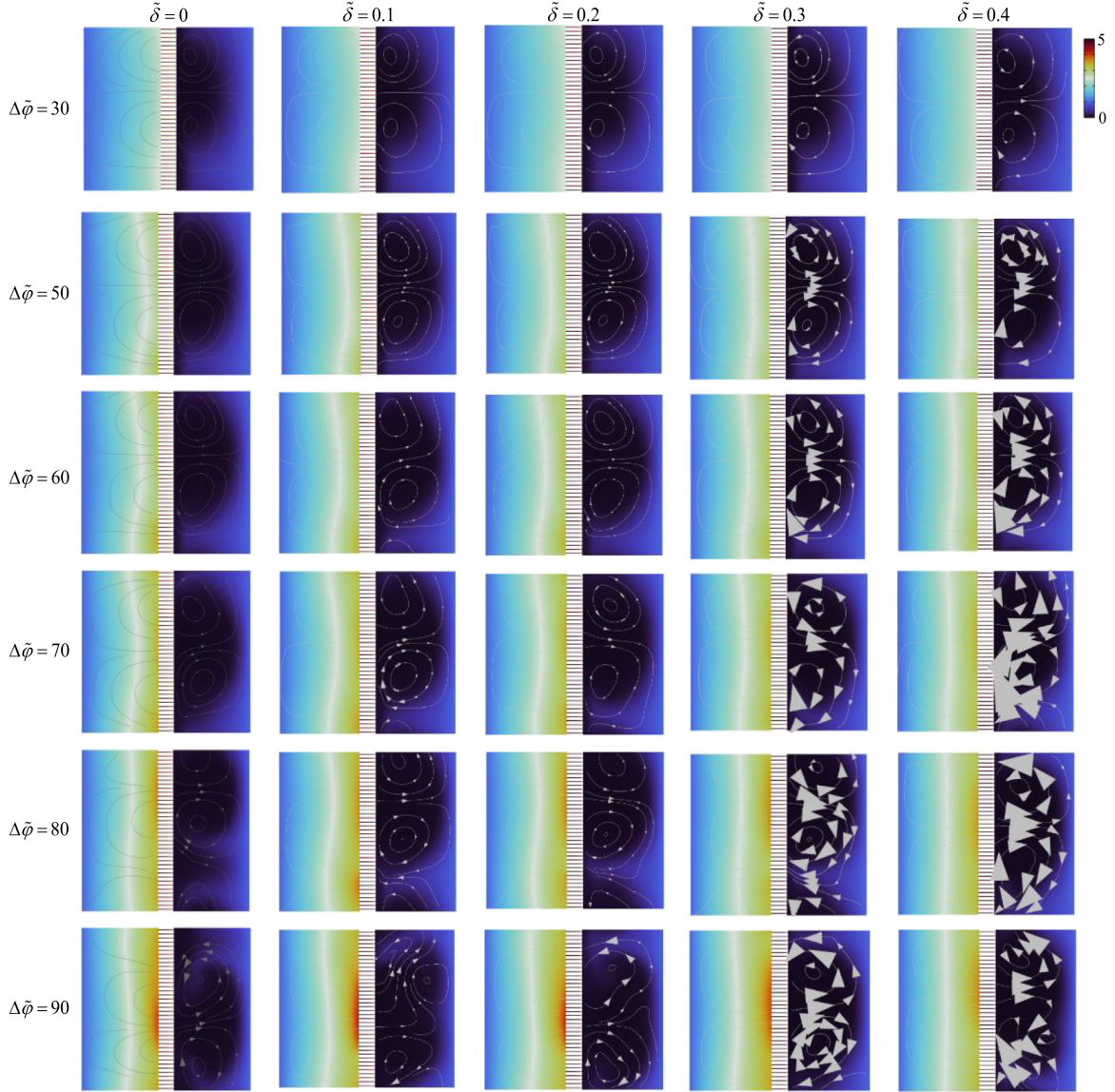


FIG. 8. Flow pattern. The impact of voltage difference and steric number on the concentration field and streamlines. As the voltage difference and steric number increase, the flow intensifies.

alteration subsequently modifies the transport characteristics within the nanoslot.

Ignoring steric effects, the interface between the membrane and solution can be described by the classical Donnan theory. Based on thermodynamic equilibrium analysis, Ref. [38] derived an analytical solution for the Donnan potential at the membrane-solution interface. The Donnan theory describes the potential difference induced by concentration gradients at the membrane-solution interface in the absence of an external electric field. Further quantitative comparison between the numerical solution presented in this paper and the analytical solution ensures the capability of our DNS to accurately capture changes in concentration gradients and potential at the membrane-solution interface:

$$\tilde{\varphi}_{\text{Donnan}} = \frac{\left[\frac{RT}{zF} \ln \left(\frac{\left(\sqrt{\left(\frac{\sigma}{zFH} \right)^2 + c_L^2} + \frac{\sigma}{zFH} \right)}{c_L} \right) \right]}{V_T}. \quad (\text{B1})$$

Here, $\tilde{\varphi}_{\text{Donnan}}$ represents the Donnan potential under zero electric field, resulting from nanoslot-bulk diffusion effects. H denotes the channel height of the nanotube. F stands for Faraday's constant, R stands for the gas constant, z represents the valency of ions, σ denotes the surface charge of the channel, c_L stands for bulk concentration, and V_T represents the thermal voltage.

The numerical solution presented in this paper aligns with the analytical solution of the Donnan potential when steric effects are neglected, as shown in Fig. 7(b). This indicates that the current model can accurately capture subtle changes in concentration gradients at the nanoslot-bulk interface.

Similar to previous studies on electroconvection (disregarding steric effects), the voltage-current curve is a response parameter in electroconvective analysis induced by flow. The voltage-current curve exhibits a three-stage relationship: as voltage increases, current initially rises linearly, then

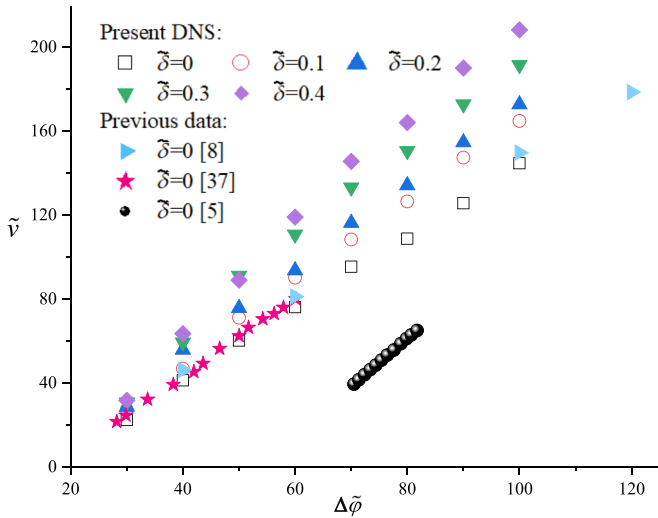


FIG. 9. The joint regulatory relation between voltage difference and steric number on the slip velocity.

reaches a saturation point. Upon surpassing a critical voltage, electroconvection initiates. Vortices drive more cations to transport at the membrane surface, forming an overlimiting current region. By conducting parameterized scans of voltage, our current simulation results are generally consistent with those in the previous data, as shown in Fig. 7(c). Through these three quantitative comparisons, we can further explore the modulating effects of steric effects on electroconvective flow.

APPENDIX C: STREAMLINES AND CONCENTRATION DISTRIBUTION

Figure 8 illustrates the influence of a wide range of voltages and steric numbers on electroconvective flow. With the increase in voltage and steric number, we observe that the arrows representing streamlines become progressively stronger, indicating enhanced flow. We indicated that steric effects resulted in reduced flow structure sizes, contributing to the presence of numerous fluctuating concentration plumes. This signifies a heightened intensity in the local vortex rolling. Conversely, in scenarios without considering steric effects, we observed larger-scale vortex structures, leading to longer durations of fluctuating concentration plumes. In simpler terms, the intensity of vortex rolling increased when accounting for steric effects.

APPENDIX D: DATA OF SLIP VELOCITY

In Fig. 9, we present the raw data in the main document. For Ref. [5], we extracted the data corresponding to fully developed EC, ranging from 1.674V to 2.13V. Normalizing

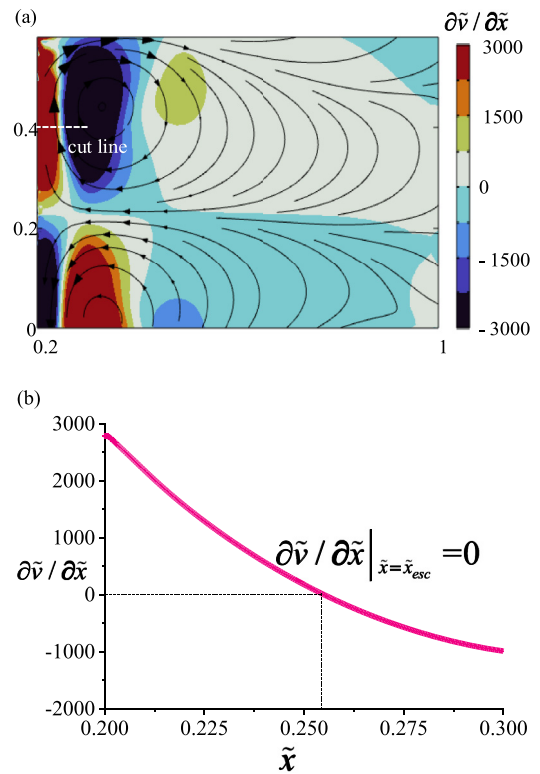


FIG. 10. (a) Spatial distribution of $\partial\tilde{v}/\partial\tilde{x}$. (b) Distribution of $\partial\tilde{v}/\partial\tilde{x}$ at the cut line ($0.2 < \tilde{x} < 0.3$, $\tilde{y} = 0.4$). Here, $\Delta\tilde{\varphi} = 100$, $\tilde{\delta} = 0.4$ and $\tilde{\tau} = 0.01$.

according to the thermal voltage and diffusion velocity as per this paper, we obtain the following dimensionless voltage and dimensionless slip velocity data. Using scaling ($\tilde{v} \sim (\alpha\tilde{\delta} + 1)^4 (\Delta\tilde{\varphi} - \tilde{\varphi}_m)$), all scattered data points are collapsed onto our scaling line, as shown in Fig. 5(a) in the main file. For Ref. [5], the threshold voltage for vortex initiation is $\tilde{\varphi}_m \approx 60$; for Ref. [37], $\tilde{\varphi}_m \approx 20$; for the solution-membrane-solution system in this paper, $\tilde{\varphi}_m \approx 21$.

APPENDIX E: VERIFICATION OF SHEAR-FREE BOUNDARY CONDITION AT OUTER EDGE OF ESC

The characteristic of electroconvection is the vortex structure, which tangentially rolls along the edge of the extended space charge layer. Consequently, the slip velocity of the vortex initiates at this edge, implying that the vortex streamlines do not penetrate the membrane. This establishes a shear-free boundary condition. To validate this analysis, we extracted our DNS results, depicted in Fig. 10(a). We delineated a cut line within the vortex region and illustrated it in Fig. 10(b). The findings reveal zero values precisely at the edge of the ESC layer.

[1] S. J. Kim, S. H. Ko, K. H. Kang, and J. Han, Direct seawater desalination by ion concentration polarization, *Nat. Nanotechnol.* **5**, 297 (2010).

[2] C.-Y. Lin, J.-P. Hsu, and L.-H. Yeh, Rectification of ionic current in nanopores functionalized with bipolar polyelectrolyte brushes, *Sensors and Actuators B* **258**, 1223 (2018).

- [3] Q. Chen, L. Xie, H. Zhu, W. Liu, Z. Jiang, Z. Zhang, D. Zhang, B. Li, and J. Ju, Insight into ettringite induced concrete crack healing by electrodeposition: Effects of electrochemical parameters and numerical simulations, *Cem. Concr. Compos.* **149**, 105504 (2024).
- [4] B. Zaltzman and I. Rubinstein, Electro-osmotic slip and electroconvective instability, *J. Fluid Mech.* **579**, 173 (2007).
- [5] S. M. Rubinstein, G. Manukyan, A. Staicu, I. Rubinstein, B. Zaltzman, R. G. H. Lammertink, F. Mugele, and M. Wessling, Direct observation of a nonequilibrium electro-osmotic instability, *Phys. Rev. Lett.* **101**, 236101 (2008).
- [6] I. Rubinstein and B. Zaltzman, Equilibrium electroconvective instability, *Phys. Rev. Lett.* **114**, 114502 (2015).
- [7] B. Xu, Z. Gu, W. Liu, P. Huo, Y. Zhou, S. M. Rubinstein, M. Z. Bazant, B. Zaltzman, I. Rubinstein, and D. Deng, Electro-osmotic instability of concentration enrichment in curved geometries for an aqueous electrolyte, *Phys. Rev. Fluids* **5**, 091701 (2020).
- [8] C. L. Druzgalski, M. B. Andersen, and A. Mani, Direct numerical simulation of electroconvective instability and hydrodynamic chaos near an ion-selective surface, *Phys. Fluids* **25**, 110804 (2013).
- [9] C. L. Druzgalski and A. Mani, Statistical analysis of electroconvection near an ion-selective membrane in the highly chaotic regime, *Phys. Rev. Fluids* **1**, 073601 (2016).
- [10] E. Karatay, M. B. Andersen, M. Wessling, and A. Mani, Coupling between buoyancy forces and electroconvective instability near ion-selective surfaces, *Phys. Rev. Lett.* **116**, 194501 (2016).
- [11] G. Ahlers, S. Grossmann, and A. D. Lohse, Heat transfer and large scale dynamics in turbulent Rayleigh-Bénard convection, *Rev. Mod. Phys.* **81**, 503 (2009).
- [12] E. A. Demekhin, N. V. Nikitin, and V. S. Shelistov, Direct numerical simulation of electrokinetic instability and transition to chaotic motion, *Phys. Fluids* **25**, 122001 (2013).
- [13] E. A. Demekhin, S. G. Amiroudine, S. Ganchenko, and N. Y. Khasmatulina, Thermo-electro-convection near charge-selective surfaces, *Phys. Rev. E* **91**, 063006 (2015).
- [14] E. A. Demekhin, V. S. Shelistov, and S. V. Polyanskikh, Linear and nonlinear evolution and diffusion layer selection in electrokinetic instability, *Phys. Rev. E* **84**, 036318 (2011).
- [15] V. S. Pham, Z. Li, K. M. Lim, J. K. White, and J. Han, Direct numerical simulation of electroconvective instability and hysteretic current-voltage response of a permselective membrane, *Phys. Rev. E* **86**, 046310 (2012).
- [16] G. Yossifon and H. C. Chang, Selection of nonequilibrium overlimiting currents: Universal depletion layer formation dynamics and vortex instability, *Phys. Rev. Lett.* **101**, 254501 (2008).
- [17] Y. Green and G. Yossifon, Dynamical trapping of colloids at the stagnation points of electro-osmotic vortices of the second kind, *Phys. Rev. E* **87**, 033005 (2013).
- [18] G. Yossifon and H.-C. Chang, Changing nanoslot ion flux with a dynamic nanocolloid ion-selective filter: Secondary overlimiting currents due to nanocolloid-nanoslot interaction, *Phys. Rev. E* **81**, 066317 (2010).
- [19] S. Kang and R. Kwak, Pattern formation of three-dimensional electroconvection on a charge selective surface, *Phys. Rev. Lett.* **124**, 154502 (2020).
- [20] R. Kwak, V. S. Pham, K. M. Lim, and J. Han, Shear flow of an electrically charged fluid by ion concentration polarization: Scaling laws for electroconvective vortices, *Phys. Rev. Lett.* **110**, 114501 (2013).
- [21] R. Kwak, V. S. Pham, and J. Han, Sheltering the perturbed vortical layer of electroconvection under shear flow, *J. Fluid Mech.* **813**, 799 (2017).
- [22] W. Liu, Y. T. Zhou, and P. P. Shi, Shear electroconvective instability in electro dialysis channel under extreme depletion and its scaling laws, *Phys. Rev. E* **101**, 043105 (2020).
- [23] W. Liu, Y. T. Zhou, and P. P. Shi, Critical selection of shear sheltering in electroconvective flow from chaotic to steady state, *J. Fluid Mech.* **946**, A3 (2022).
- [24] G. Li, L. A. Archer, and D. L. Koch, Electroconvection in a viscoelastic electrolyte, *Phys. Rev. Lett.* **122**, 124501 (2019).
- [25] J. Cai, D. Zhao, and G. Li, Direct numerical simulation of electroconvection under a uniform magnetic field, *Phys. Rev. Fluids* **8**, 113701 (2023).
- [26] W. Liu, Y. Zhou, and P. Shi, Sheltering electroconvective instability in a weak electrolyte, *Phys. Fluids* **33**, 072011 (2021).
- [27] H. J. Kwon, B. Kim, G. Lim, and J. Han, A multiscale-pore ion exchange membrane for better energy efficiency, *J. Mater. Chem. A* **6**, 7714 (2018).
- [28] A. Esfandiar, B. Radha, F. C. Wang *et al.*, Size effect in ion transport through angstrom-scale slits, *Science* **358**, 511 (2017).
- [29] I. Borukhov, D. Andelman, and H. Orland, Steric effects in electrolytes: A modified Poisson-Boltzmann equation, *Phys. Rev. Lett.* **79**, 435 (1997).
- [30] Z. Seifollahi and S. N. Ashrafzadeh, Ionic-size dependent electroosmotic flow in ion-selective biomimetic nanochannels, *Colloids Surf. B* **216**, 112545 (2022).
- [31] B. D. Storey, L. R. Edwards, M. S. Kilic, and M. Z. Bazant, Steric effects on ac electro-osmosis in dilute electrolytes, *Phys. Rev. E* **77**, 036317 (2008).
- [32] W. Y. Zhang, X. Xi, Liu, K. Jiao, Q. W. Wang, C. Yang, and C. L. Zhao, Ion steric effect induces giant enhancement of thermoelectric conversion in electrolyte-filled nanochannels, *Nano Lett.* **23**, 8264 (2023).
- [33] M. S. Kilic and M. Z. Bazant, Steric effects in the dynamics of electrolytes at large applied voltages. II. Modified Poisson-Nernst-Planck equations, *Phys. Rev. E* **75**, 021503 (2007).
- [34] H. Daiguji, P. D. Yang, and A. Majumdar, Ion transport in nanofluidic channels, *Nano Lett.* **4**, 137 (2004).
- [35] Y. Green, Ion transport in nanopores with highly overlapping electric double layers, *J. Chem. Phys.* **154**, 084705 (2021).
- [36] E. Dydek, B. Zaltzman, I. Rubinstein *et al.*, Overlimiting current in a microchannel, *Phys. Rev. Lett.* **107**, 118301 (2011).
- [37] Y. Zhang, Y. M. Zhang, K. Luo, H. L. Yi, and J. Wu, Electroconvective instability near an ion-selective surface: A mesoscopic lattice Boltzmann study, *Phys. Rev. E* **105**, 055108 (2022).
- [38] H. Tian, L. Zhang, and M. Wang, Applicability of Donnan equilibrium theory at nanochannel-reservoir interfaces, *J. Colloid Interface Sci.* **452**, 78 (2015).